Supplementary Information

Quantitative Determination the Role of the Intra-bandgap States in Water Photooxidation over Hematite Electrodes

*Shufeng Zhang, Wenhua Leng**

Department of Chemistry, Zijingang Campus, Zhejiang University, Hangzhou, Zhejiang 310058, China

Table of contents

1 Brief summary of the intra-bandgap states study on hematite photoanodes ...3

2 Theory background 4

2.1 Intra-bandgap states measurements 4

2.2 Theoretic model of intra-bandgap states mediating charge transfer and recombination 7

3 Photoanodes preparation 10

4 Photoanodes characterization 10

* Corresponding Author. E-mail: lengwh@zju.edu.cn;

4.1 (Photo)-electrochemical measurements 10

4.2 Spectroelectrochemical measurement 11

4.3 Transient absorption spectroscopy (TAS) measurements 11

5 Photoelectrochemical performance measurements results 13

6 Mott-Schottky results 14

7 Measurements of the intra-bandgap state 18

8 *I-V* curves in the presence of hole scavenger Na_2SO_3 23

9 Spectroelectrochemistry results of hematite photoanode reported in the literatures 25

10 Cyclic voltammetry (CV) measurements 27

11 Transient absorption spectroscopy (TAS) results 29

12 Electrochemical impedance spectroscopy (EIS) results 30

1 Brief summary of the study on the intra-bandgap states on hematite photoanodes

Supplementary Table 1. Brief summary of the study on the intra-bandgap states on hematite photoanodes

	Method	Types	Role	Chemical identity	Density	Energy level	Ref
Theoretic calculations	DFT[a]	**2**	SS1: Rec center SS2:CT center	SS1 Fe-OH SS2 Fe-O·	/	/	1
		1	CT center	Fe-O·	/	/	2
Optical experiments	SEC[b]	**1**	CT center	/	/	/	3, 4, 5
		1	Rec center	/	/	/	6
	TAS[c]	**1**	Rec center	/	/	/	7, 8, 9
	PIAS[d]	**1**	Rec center	/	/	/	10
	NEXAFS[e]	**2**	/	/	/	/	11
	ATR-IRs[f]	**1**	CT center	Fe^{IV}=O	/	/	12
Electrical experiments	CV[g]	**1**	CT center	/	~17 μC cm^{-2}	/	5
	EIS[h]	**2**	SS1: Rec center SS2: CT center	/	SS2:~150 μF cm^{-2}	1.3 V_{RHE}	13
		1	CT center	/	~155 μF cm^{-2}	1.3 V_{RHE}	14
		2	Both SS1 and SS2 are CT center, and interplay	/	SS1:~24 μF cm^{-2} SS2:~16 μF cm^{-2}	SS1:~0.8 $V_{RHE;}$ SS1:~1.4 $V_{RHE;}$	15
		2	SS1:Rec center SS2: CT center	/	SS1:~100 μF cm^{-2}	SS1:~0.64 $V_{RHE;}$	16

	IMPS[i]	**1**	CT center	/	SS2:~70 μF cm^{-2}	SS1:~1.04 $V_{RHE;}$	17

Note:[1]. the explanation for the shorthand notations in the column of **Methods** are as follow:[a] Density functional theory; [b] Spectroelectrochemical spectroscopy; [c] Transient absorption spectroscopy; [d] Photoinduced absorption spectroscopy; [e] Near-edge X-ray absorption fine structure; [f] Infrared spectroscopy; [g] Cyclic voltammetry; [h] Electrochemical impedance spectroscopy; [i] Intensity modulated photocurrent spectroscopy.

[2]. the **SS1** or **2** are denoted as the different types of the surface state; Rec center/ CT center is denoted as recombination and charge transfer center in the column of **Role**.

2 Theory background

2.1 The measurements of the intra-bandgap states

Electrochemical impedance spectroscopy (EIS) can be used to characterize the intra-bandgap states at an n-type semiconductors as reported previously.[18, 19, 20, 21, 22] The filling and emptying of the electrically active intra-bandgap states would give rise to an additional response impedance parallel to that of the space charge layer when the applied potential changes. As a result, the measured impedance corresponded to the intra-bandgap states $C_p(\omega)$, after subtraction of space charge layer capacitance (C_{SC}), can be obtained from the real (Re(Z)) and imaginary (Im(Z)) parts of the measured impedance, as shown in **Supplementary eq.(1)** and **(2)**.[18, 19]

$$C_{\mathrm{p}}(E_{\mathrm{appl}}, \omega) = [\omega Im(\mathrm{Z})(1 + D^2)]^{-1} - C_{\mathrm{sc}} \quad (1)$$

$$D = [\frac{Re(Z) - R_{\mathrm{S}}}{-Im(Z)}] \quad (2)$$

According to previous report[19], for those intra-bandgap states interacting only with the conduction band which may be observed both in the dark and under illumination as illustrated in **Supplementary Figure 1**a, the $C_{\mathrm{p}}(\omega)$ is described by **Supplementary eq.(3)**, where k_{sr} is the surface recombination rate constant of these intra-bandgap states with the electron at conduction band, $k_{\text{-sr}}$ is the rate constant of the electron detrapping from the intra-bandgap states into the conduction band, ω is angular frequency, S_{tot} is the density of the intra-bandgap states, q is the elementary charge, k_{B} is the Boltzmann constant, and T is the temperature .

$$C_{\mathrm{p}}(\omega) = \frac{q^2}{k_{\mathrm{B}}T} \frac{k_{\mathrm{sr}} k_{-\mathrm{sr}}}{\omega^2 + (k_{\mathrm{sr}} + k_{-\mathrm{sr}})^2} S_{\mathrm{tot}} \quad (3)$$

From **Supplementary eq.(3)**, at low frequencies, a frequency-dependent maximum in capacitance (denoted as $C_{\mathrm{p}}(\max)_{\omega \to 0}$) will be observed as a function of the applied potential at:

$$k_{\mathrm{sr}} = k_{-\mathrm{sr}} \quad (4)$$

In this case, the $C_{\mathrm{p}}(\max)_{\omega \to 0}$ can be described as:

$$C_{\mathrm{p}}(\max)_{\omega \to 0} = \frac{q^2}{4k_{\mathrm{B}}T} S_{tot} \quad (5)$$

Consequently, S_{tot} can be determined from the $C_{\mathrm{p}}(\max)_{\omega \to 0}$ when plotting $C_{\mathrm{p}}(\omega)$ *vs.* applied potential (implicit in k_{sr}) for various frequencies.

Similarly, if the intra-bandgap states function as recombination center for the photocarriers as illustrated in **Supplementary Figure 1**b, the density of the occupied

states (S_{tot}^{-}) is given by **Supplementary eq.(6)** and the $C_{\mathrm{p}}(\omega)$ is described by **Supplementary eq.(7)**:[19]

$$S_{\mathrm{tot}}^{-} = \frac{k_{\mathrm{sr}}}{(k_{\mathrm{trap}}+k_{\mathrm{sr}})} S_{\mathrm{tot}} \tag{6}$$

$$C_{\mathrm{p}}(\omega) = \frac{q^2}{k_{\mathrm{B}}T} \frac{(k_{\mathrm{sr}})^2 k_{\mathrm{trap}}}{(k_{\mathrm{sr}}+k_{\mathrm{trap}})} \frac{S_{\mathrm{tot}}}{\omega^2+(k_{\mathrm{sr}}+k_{\mathrm{trap}})^2} \tag{7}$$

Where k_{trap} is the rate constant of photohole trapped in the intra-bandgap states.

At low frequencies, $C_{\mathrm{p}}(\max)_{\omega\to 0}$ can be found in the plots of $C_{\mathrm{p}}(\omega)$ *vs.* applied potential approximately at the potential, where:

$$k_{\mathrm{sr}} = k_{\mathrm{trap}} + \sqrt{(k_{\mathrm{trap}})^2 + \omega^2} \tag{8}$$

For the low frequency limit ($\omega\to 0$), **Supplementary eq.(8)** can be approximated to be:

$$k_{\mathrm{sr}} = 2k_{\mathrm{trap}} \tag{9}$$

In this case, **Supplementary eq.(6)** and **Supplementary eq.(7)** can be described by:

$$S_{\mathrm{tot}}^{-} = \frac{2}{3} S_{\mathrm{tot}} \tag{8}$$

$$C_{\mathrm{p}}(\max)_{\omega\to 0} = \frac{4q^2}{27k_{\mathrm{B}}T} S_{\mathrm{tot}} \tag{9}$$

From **Supplementary eq.(9)**, the density of the recombination centers, S_{tot}, can be obtained from the maximum capacitance, $C_{\mathrm{p}}(\max)_{\omega\to 0}$.

Meanwhile, if these intra-bandgap states simultaneously involves with the charge transfer processes in addition to serve as recombination center as illustrated in **Supplementary Figure 1**c, a kinetic model of surface states mediated charge transfer and recombination can be proposed for water oxidation at the irradiated hematite

electrode[20, 21, 22], which will be introduced in details below.

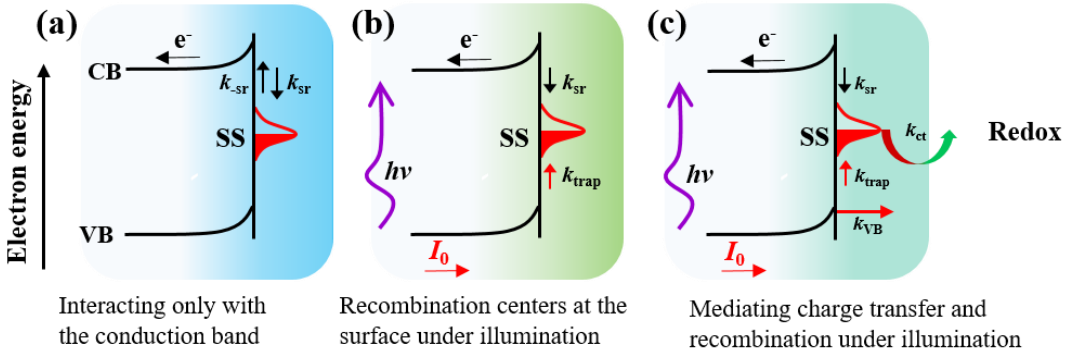

Supplementary Figure 1. Energy-band diagrams showing processes at the hematite and electrolyte interface **(a)** intra-bandgap states interacting only with the conduction band, which may be observed both in the dark and under illumination; and **(b)** recombination centers at the surface under illumination; **(c)** intra-bandgap states mediating charge transfer and recombination under illumination.

2.2 Theoretic model of intra-bandgap states mediating charge transfer and recombination

Generally, the elemental processes for water photooxidation at an n-type semiconductors are schematically illustrated in **Supplementary Figure 1**c. Upon illumination, the absorbed photons will create electron-hole pairs in the electrodes. A part of photogenerated holes after escaping the bulk recombination move to the surface, generating a photohole flux, in terms of current, I_0 where they can transfer directly from

valence band to any surface complex with the rate constant k_{VB}. However, it is suggested the probability of direct hole transfer from the valence band to the electrolyte should be very low due to the absence of a one-electron redox couple in the electrolyte[20, 23, 24]. Thus, the k_{VB} process is neglected in this model. Alternatively, holes reached at the electrode surface can be captured by the intra-bandgap states (located at an energy level E_{ss}, with a density of S_{tot}) with the rate constant k_{trap}. Holes captured at the intra-bandgap states can transfer to electron donors with the rate constant k'_{ct} or recombine with electrons with the rate constant k'_{sr}. We introduce at this point the shorthand notations, $k_{ct} = k'_{ct}[D]$ and $k_{sr} = k'_{sr}n_s$, where n_s is the electron density at the surface.

In this model, the applied potential (φ) across the semiconductor liquid junction (SCLJ) is regarded to be distributed between the part of the space charge layer (φ_{SC}) and that of the Helmholtz layer (φ_H). As a result, the potential dependent surface recombination rate constant k_{sr} and charge transfer rate constant k_{ct} can be described as follow:

$$k_{sr} = k'_{sr}n_s = k^0_{sr}\exp(\frac{-\alpha q\varphi_{SC}}{\kappa_B T}) \quad (10)$$

$$k_{ct} = k^0_{ct}\exp(\frac{\beta q\varphi_H}{\kappa_B T}) \quad (11)$$

Where n_s is the surface density of electrons, k^0_{sr} is the value of k_{sr} at $\varphi_{SC} = 0$, α is the ideality factor, q is the elementary charge, k_B is the Boltzmann constant, and T is the temperature. k^0_{ct} is the value of k_{ct} at $\varphi_H = 0$, β is the charge transfer coefficient.

The rate constant k_{trap} is assumed to be independent on the potential drop in the depletion layer.[20]

Based on the continuity equation as reported previously[20, 25], the steady state concentration of photohole accumulated in the surface state, p_{ss}^0 and photocurrent, j_{st} can be described as **Supplementary eq.(12)** and **(13)**, respectively.

$$p_{ss}^0 = \frac{I_0}{(k_{ct}+k_{sr})} \quad (12)$$

$$j_{st} = k_{ct}p_{ss}^0 = \frac{k_{ct}I_0}{(k_{ct}+k_{sr})} \quad (13)$$

Based on this model, a theoretic impedance expression for water photooxiation on the photoanodes can be derived. Analysis of the theoretic impedance expression gives the relationship of k_{ct} and characteristic frequency (ω_{max}^1) at the low frequency: [20]

$$\omega_{max}^1 = k_{ct}\left[1 + \frac{C_{SC}}{C_H} + \frac{\beta q I_0}{\kappa_B T C_H (k_{ct}+k_{sr})}\right] = k_{ct}\left(1 + \frac{C_{SC}}{C_H}\right) + \frac{j_{st}\beta q}{\kappa_B T C_H} \quad (14)$$

It shows that the ω_{max}^1 is affected by 3 parts:**1)** the first part is caused by the potential drop on space charge layer φ_{SC}; **2)** the potential drop across the Helmholtz layer φ_H; **3)** the accumulation of photoholes on the surface states. Therefore, as long as the $C_{SC}/C_H + \beta q p_{ss}^0/\kappa_B T C_H \ll 1$ is not satisfied, k_{ct} is expected to be potential and light intensity dependent in the EIS response. On the other hand, if the applied potential only drops on the space charge layer (for the case $C_{SC} \ll C_H$) and the effect of the photohole accumulation can be ignored completely (for the case $I_0 \ll C_H(k_{ct} + k_{sr})\kappa_B T/\beta q$), then, k_{ct} would be constant as described in **Supplementary eq.(15)**:[20]

$$\omega_{max}^1 = k_{ct} \quad (15)$$

Besides, under high light intensity (for the case, $I_0 \gg C_H(k_{ct} + k_{sr})\kappa_B T/\beta q$), it

is predicted that ω_{max}^{1} is proportional to j_{st}, as given in **Supplementary eq.(16)**.[20]

$$\omega_{max}^{1} = \frac{\beta q k_{ct} I_0}{\kappa_B T C_H (k_{ct}+k_{sr})} = \frac{\beta q}{\kappa_B T C_H} j_{st} \quad (16)$$

The above theoretic predictions allow us to verify the rationality of the model.

3 The preparation of the photoanodes

The processes for the preparation of the photoanodes were the same as previous reports[26, 27], but with a slight modification of the rate of spin-coating. Generally, the precursor solution, which contains 60 mM $FeCl_3$ in the ethanol, was dispersed into the indium-doped tin oxide (ITO) conducting glass by spin-coating. The coated glass was dried at the room temperature and subsequently heated in a muffle furnace (Nabertherm, N7/H, Germany) in air at 350 °C for 5 min. This procedure was repeated eight times and then the film was annealed in air at 550 °C for 4 h.

4 The characterization of the Photoanodes

4.1 (Photo)-electrochemical measurements

The (photo-)electrochemical experiments were performed in a conventional three-electrode cell as reported previously[28]. The film electrode was used as a working electrode, a large surface area of Pt mesh as a counter electrode and all potentials were measured against a calomel reference electrode (SCE). The electrolyte was aqueous solution of 1 M NaOH (pH 13.8) and different pHs of 8.2, 10.1, 12.0 for the electrolyte are adjusted by adding $HClO_4$. To keep oxygen free, all electrolyte were purged with nitrogen prior experiment. The electrochemical station (Reference 600, Gamry Co. Ltd.,

USA) was used as constant voltage source. For illumination condition, the light source was 150 W xenon lamp coupled with an AM 1.5 global filter (Newport 81094). The illuminated surface area of films was 1 cm^2. The light was incident from the electrolyte-electrodes side. All potentials were measured with respect to SCE in the text unless otherwise specified.

The EIS measurements for the k_{ct} derivation were the same as described previously[21]. The Mott-Schottky experiments were performed under illumination and other experimental conditions were the same as that in prior report[21]. Impedance measurements for analysis of intra-bandgap states were the similar to the Mott-Schottky experiments, with a 3 mV (rms) amplitude at changing frequencies.

4.2 Spectroelectrochemical measurement

The spectroelectrochemical measurement was conducted on a UV-Vis spectrometer (UV-7502, Shanghai Xinmao Instruments Co., Ltd., China) where the three-electrode cell setup as described above was placed inside the UV-vis chamber. The optical absorption signals were recorded at different applied potential which is controlled by the electrochemical station (CHI 630b, Shanghai Chenhua Co., Ltd., China).

4.3 Transient absorption spectroscopy (TAS) measurements

Transient absorption measurements were the same as reported previously[21, 22]. In general, the measurement were performed on a home-modified laser flash photolysis

spectrometer (LP920, Edinburgh Instruments Ltd., U.K.). A Nd:YAG laser (Opolette 355 LD-HE, 355 nm, 7 ns pulse width) operating at 1 Hz was the UV excitation source. Care was taken to ensure that the entire immersed area of the electrodes was irradiated by the UV excitation source. The repetition rate was chosen to ensure that all charge carriers had fully decayed prior to the next excitation event. The wavelength of the probe light (150 W tungsten halogen lamp, Beijing Yonghe Ganzhi Ltd., China) was selected by using two monochromators placed prior to and after the sample. The probe light was detected with a preamplifier Si photodiode (Mk2, Costronics Electronics, U.K.), and the detected signal was sent to the main amplification system with an electronic band-pass filter (Costronics Electronics 2015) to improve the signal-to-noise ratio. The amplified signal was recorded with a 100 MHz oscilloscope (Tektronix TDS3012C), which was synchronized with a trigger signal of the laser pulse. The detected transient absorbance ΔOD was controlled to be small as possible by adjusting the laser intensity. The data shown were the result of averaging between 100 and 200 laser shots per trace.

5 Photoelectrochemical performance measurements results

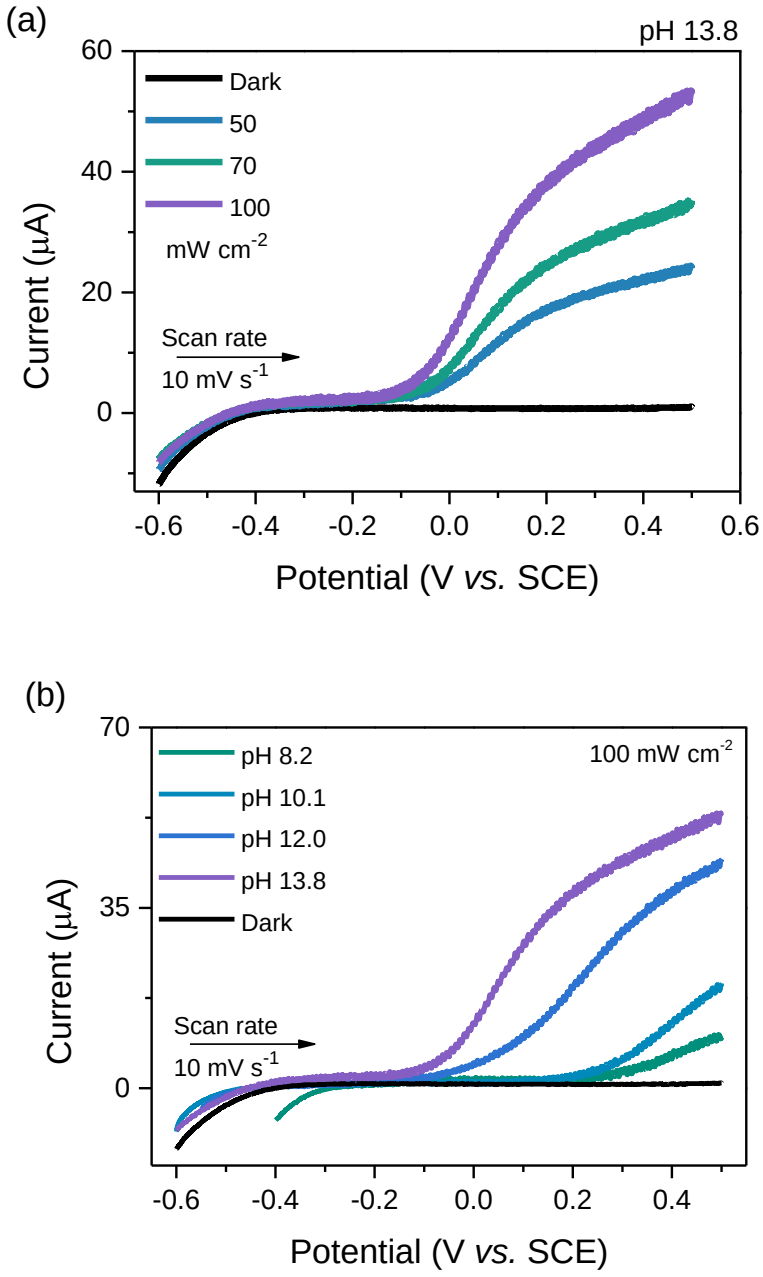

Supplementary Figure 2. Photoelectrochemcial performance. *I-V* curves of the α-Fe_2O_3 photoanodes. **(a)** in the dark and under illumination of different light intensities (50, 70, 100 mW cm^{-2}) in 1.0 M NaOH deoxygenated aqueous solution; **(b)** in the dark and under illumination of 100 mW cm^{-2} in different pHs (8.2, 10.1, 12.0) in 1.0 M NaOH deoxygenated aqueous solution.

6 Mott-Schottky results

Mott-Schottky measurements are conducted to obtain the flatband potential (E_{fb}) of the α-Fe_2O_3 electrodes. In the dark, the E_{fb} is -0.62 V_{SCE} for the electrode in 1 M NaOH solution as shown in **Supplementary Figure 3**a, in good agreement with previous reports.[29, 30] Besides, the E_{fb} under changing pH approximately satisfies the Nernstian equation with a slope of -68 mV/pH unit (**Supplementary Figure 3**b-d). Under illumination, the E_{fb} is shifted positively with the increasing light intensity and gradually saturated at high light intensity (**Supplementary Figure 3**a). This manifests that there are positive charge trapped in the electrode surface and the saturation at the high light intensity suggests a limitation for the positive charge storage at the electrode surface. As such the density of the trapped photoholes (N_{trap}) on the electrodes can be estimated from the limitation on E_{fb} shift according to **Supplementary eq.(17)**. Given that the maximum shift of the E_{fb} is ~0.067 V_{SCE} and the Helmholtz capacitance (C_H) is assumed to be 120 μF cm^{-2}, N_{trap} is estimated to be 5.05×10^{13} cm^{-2}.

$$\mathrm{d}E_{\mathrm{fb}} = -\mathrm{d}\Delta\varphi_{\mathrm{H}} = \frac{qN_{\mathrm{trap}}}{C_{\mathrm{H}}} \tag{17}$$

Where φ_H is the potential drop on the Helmholtz layer, q is the elementary charge.

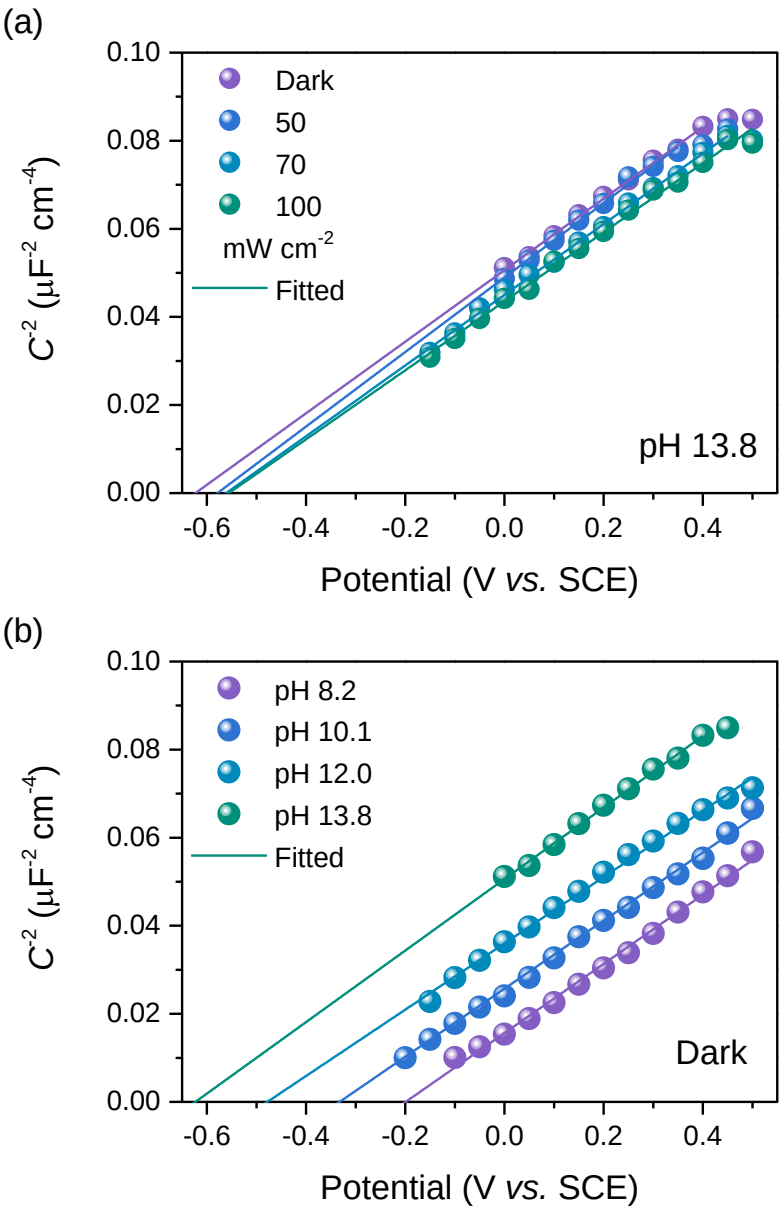
(a)
0.10
0.08
0.06
0.04
0.02
0.00
C^{-2} (μF^{-2} cm^{-4})
Dark
50
70
100
mW cm^{-2}
Fitted
pH 13.8
-0.6
-0.4
-0.2
0.0
0.2
0.4
Potential (V *vs.* SCE)
(b)
0.10
0.08
0.06
0.04
0.02
0.00
C^{-2} (μF^{-2} cm^{-4})
pH 8.2
pH 10.1
pH 12.0
pH 13.8
Fitted
Dark
-0.6
-0.4
-0.2
0.0
0.2
0.4
Potential (V *vs.* SCE)

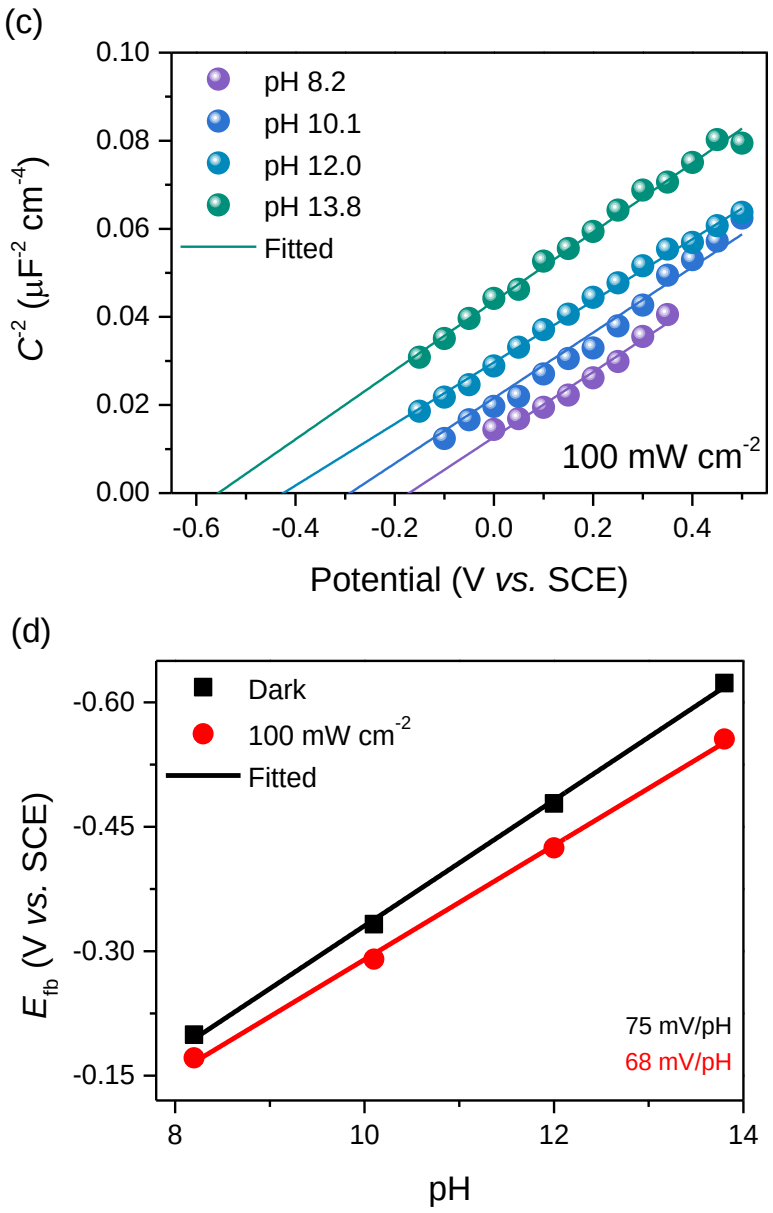
(c)
0.10
0.08
0.06
0.04
0.02
0.00
C^{-2} (μF^{-2} cm^{4})
pH 8.2
pH 10.1
pH 12.0
pH 13.8
Fitted
100 mW cm^{-2}
-0.6
-0.4
-0.2
0.0
0.2
0.4
Potential (V *vs.* SCE)
(d)
-0.60
-0.45
-0.30
-0.15
E_{fb} (V *vs.* SCE)
Dark
100 mW cm^{-2}
Fitted
75 mV/pH
68 mV/pH
8
10
12
14
pH

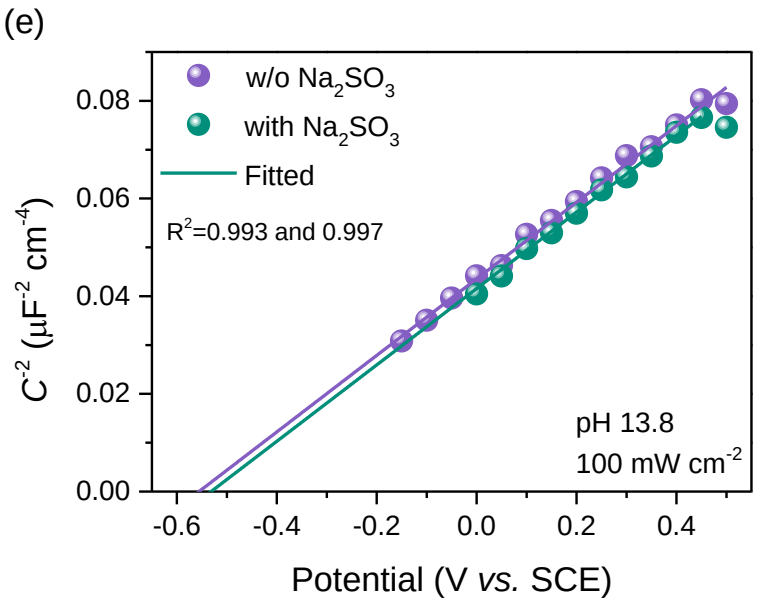

Supplementary Figure 3. Mott-Schottky plots of α-Fe_2O_3 electrode. **(a)** in the dark and under illumination of different light intensities (50, 70, 100 mW cm^{-2}) in deoxygenated 1 M NaOH (pH 13.8); the electrolyte of different pHs (8.2, 10.1, 12.0, 13.8) in the dark **(b)** and under illumination at 100 mW cm^{-2} **(c)**; the pH dependent E_{fb} in the dark and under illumination at 100 mW cm^{-2} **(d)**; **(e)** comparison of Mott-Schottky plots of α-Fe_2O_3 electrode in 1 M NaOH (pH 13.8) at 100 mW cm^{-2} without and with the addition of efficient hole scavenger [Na_2SO_3] = 30 mM. The measured frequency is 1 kHz.

7 Measurements of the intra-bandgap state

(a) pH 13.8

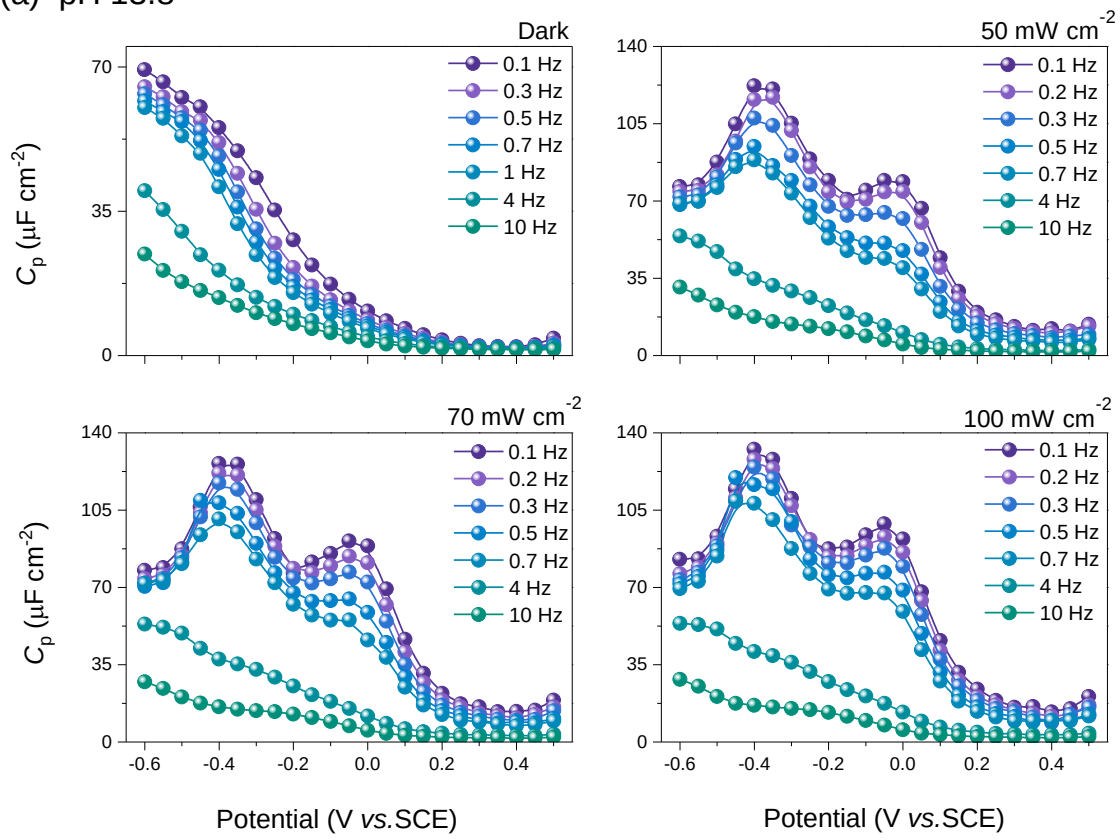

(b) pH 13.8

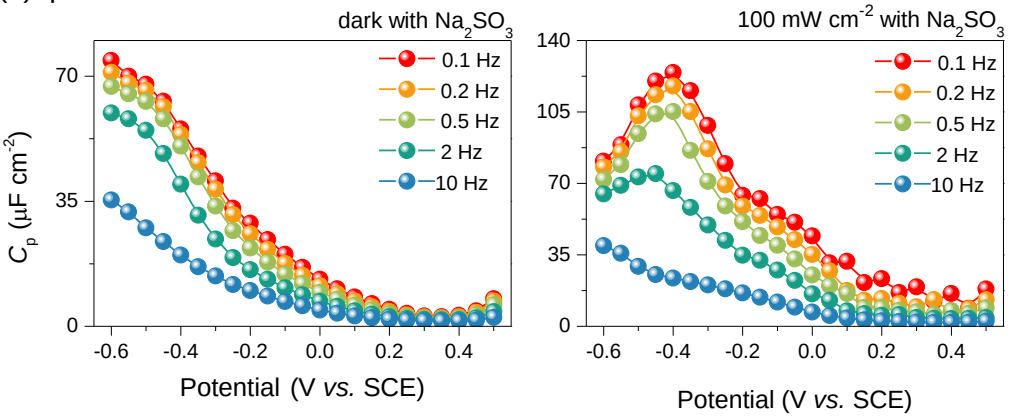

(c) pH 12.0

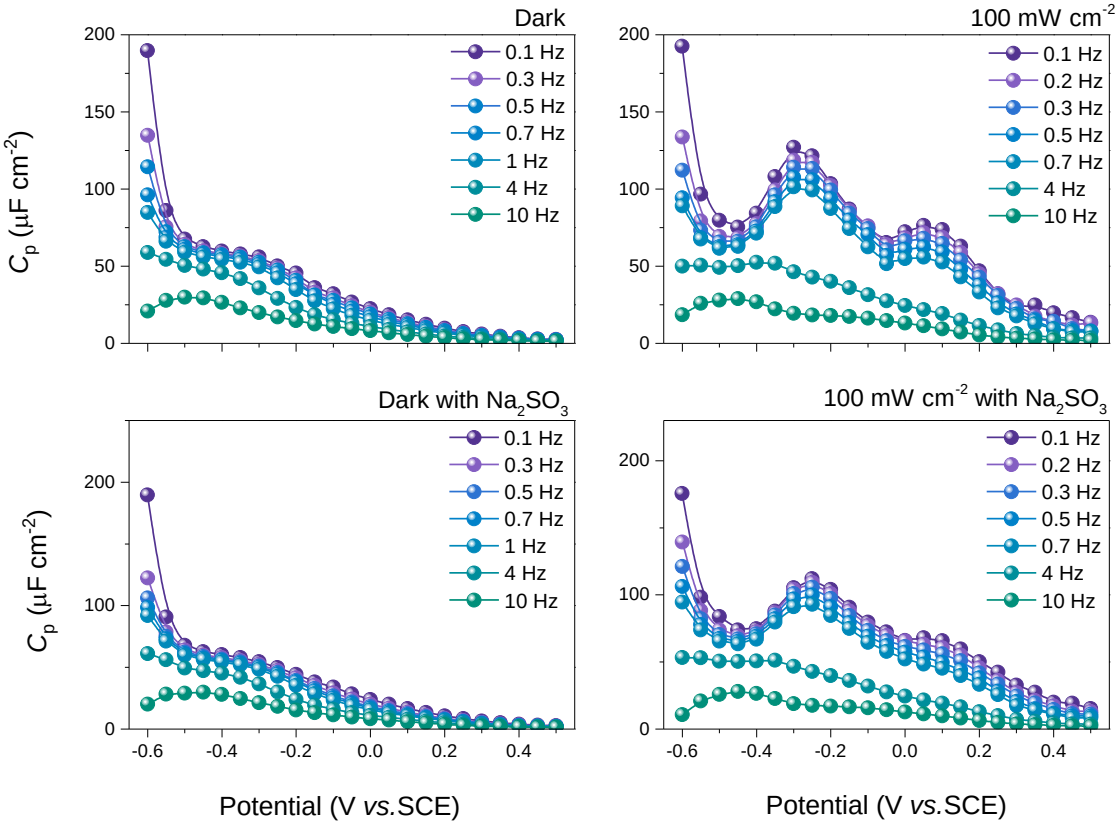
Dark
100 mW cm-2
Dark with Na2SO3
100 mW cm-2 with Na2SO3
0.1 Hz
0.2 Hz
0.3 Hz
0.5 Hz
0.7 Hz
1 Hz
4 Hz
10 Hz
Cp (μF cm-2)
Potential (V vs.SCE)

(d) pH 10.1

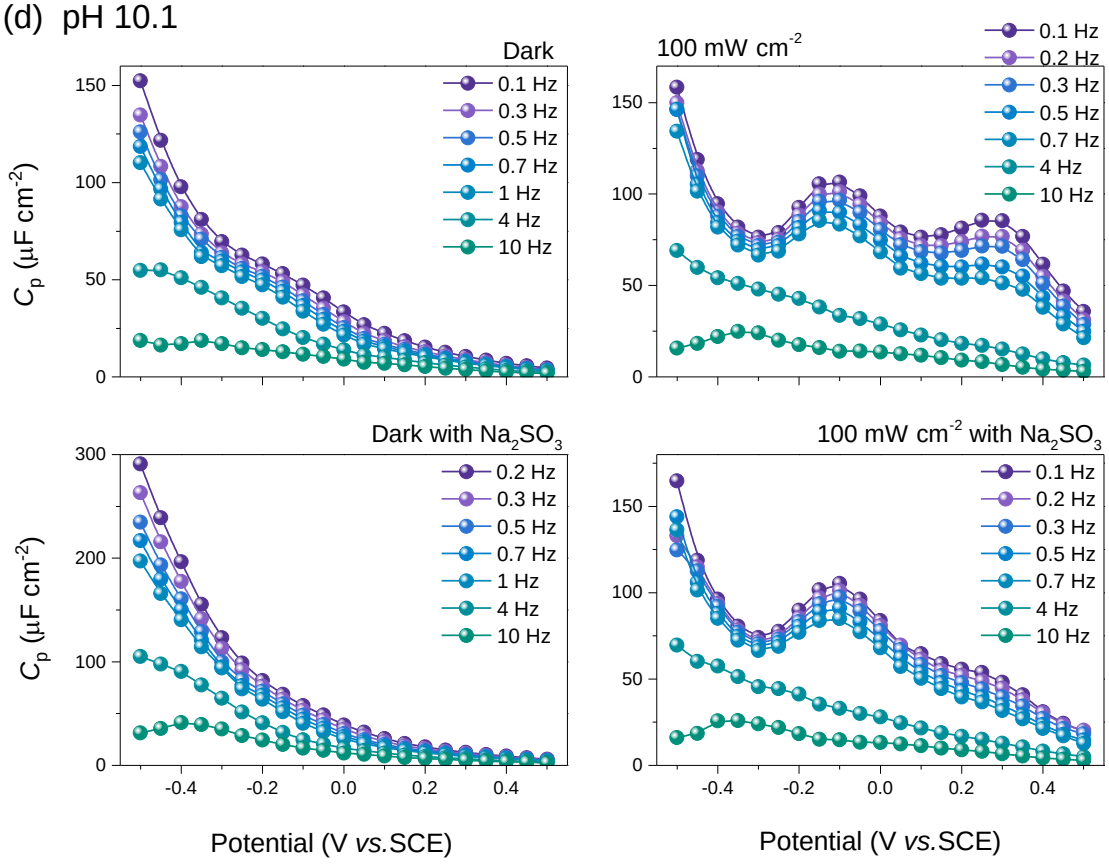
Dark
100 mW cm-2
Dark with Na2SO3
100 mW cm-2 with Na2SO3
0.1 Hz
0.2 Hz
0.3 Hz
0.5 Hz
0.7 Hz
1 Hz
4 Hz
10 Hz
Cp (μF cm-2)
Potential (V vs.SCE)

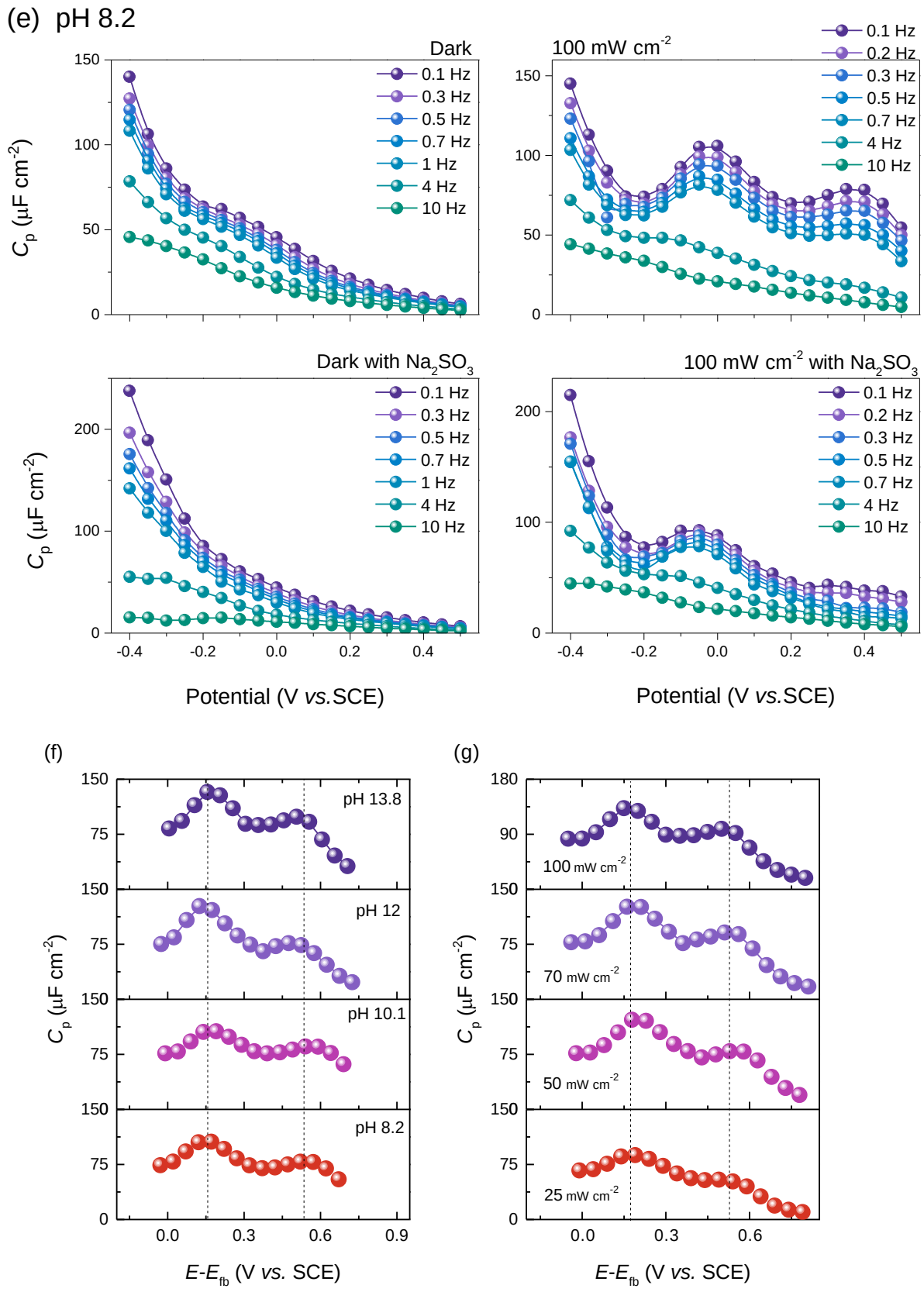

Supplementary Figure 4. Electrochemical measurements of the intra-bandgap

states. (a) curves of parallel capacitance $C_p(\omega)$ after subtraction of the space charge capacitance versus with varying applied potential (E) at different frequencies in the dark and under illumination of different light intensities (50, 70, 100 mW cm^{-2}); **(b)** $C_p(\omega)$ *vs. E* curves with the addition of efficient hole scavenger [Na_2SO_3] = 30 mM in the dark and under 100 mW cm^{-2} at different frequencies; $C_p(\omega)$ *vs. E* curves for different frequencies in the dark and under illumination 100 mW cm^{-2} without and with the efficient hole scavenger [Na_2SO_3] = 30 mM: **(c)** pH 12.0; **(d)** pH 10.1; **(e)** pH 8.2; **(f)** $C_p(\omega)$ *vs. E* curves at 0.1 Hz of different pH (8.2, 10.1, 12.0, 13.8) at 100 mW cm^{-2} with respect to corresponding E_{fb}; **(g)** $C_p(\omega)$ *vs. E* curves at 0.1 Hz of different light intensities (25, 50, 70, 100 mW cm^{-2}) at pH13.8 with respect to corresponding E_{fb}.

8 *I-V* curves in the presence of hole scavenger Na_2SO_3

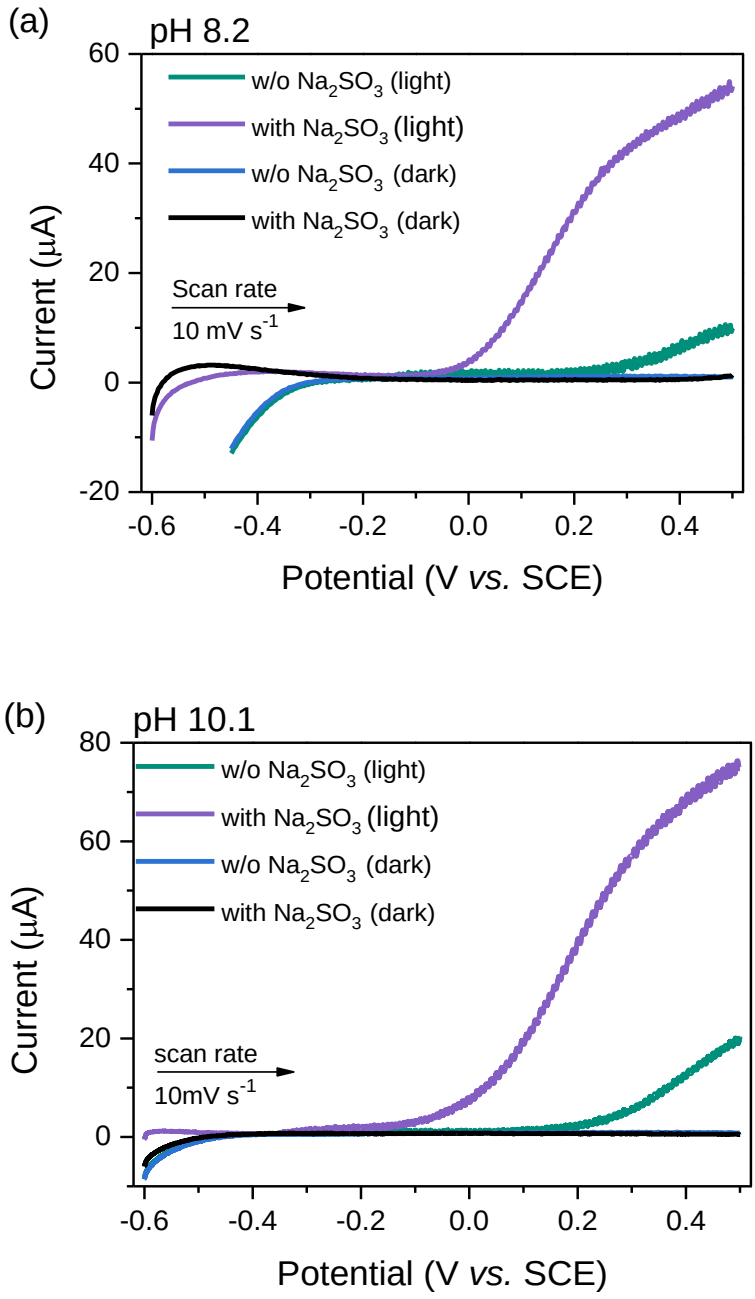

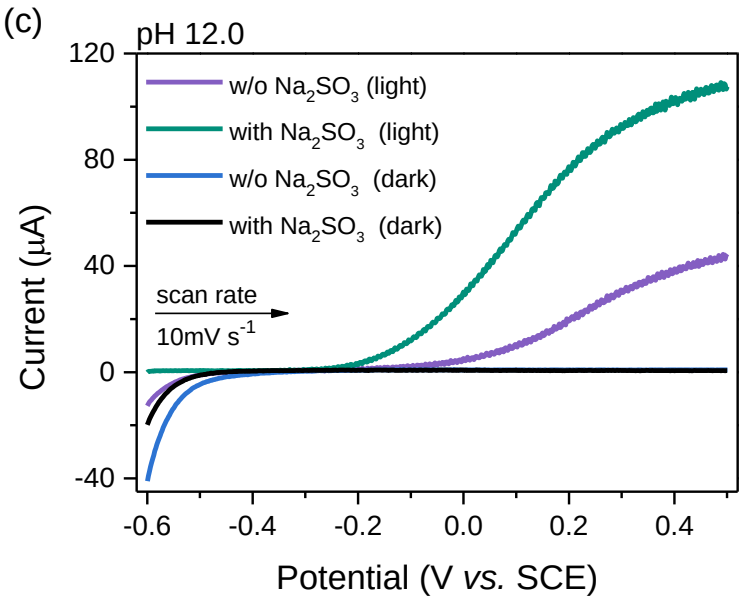

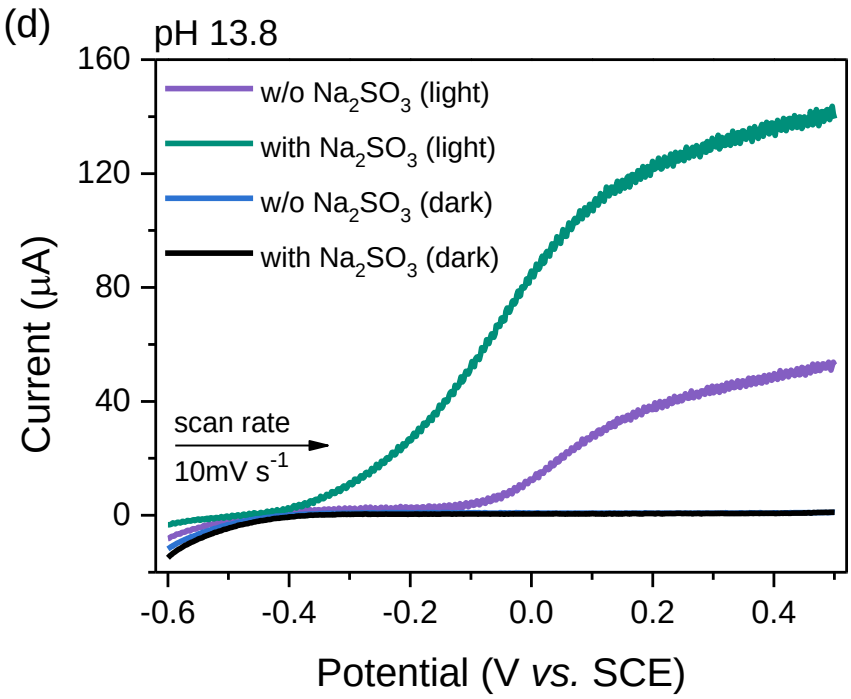

Supplementary Figure 5. *I-V* curves of the α-Fe_2O_3 photoanodes without and with the addition of efficient hole scavenger [Na_2SO_3] = 30 mM in the dark and under illumination 100 mW cm^{-2}.**(a)-(d)** pH 8.2, 10.1, 12.0, 13.8.

9 Spectroelectrochemistry results of hematite photoanode reported in the literatures

(a)

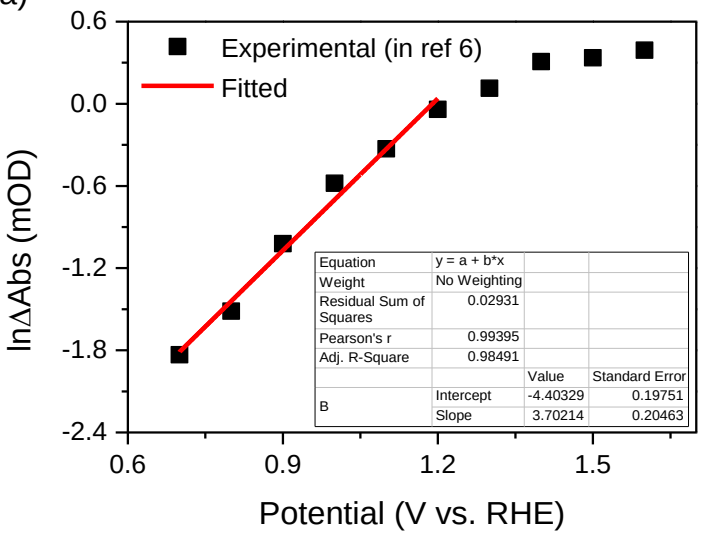

Equation	y = a + b*x		
Weight	No Weighting		
Residual Sum of Squares	0.02931		
Pearson's r	0.99395		
Adj. R-Square	0.98491		
		Value	Standard Error
B	Intercept	-4.40329	0.19751
	Slope	3.70214	0.20463

(b)

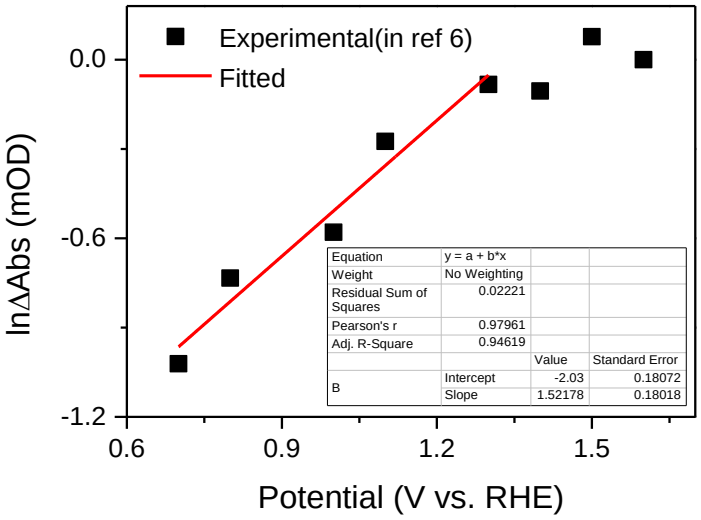

Equation	y = a + b*x		
Weight	No Weighting		
Residual Sum of Squares	0.02221		
Pearson's r	0.97961		
Adj. R-Square	0.94619		
		Value	Standard Error
B	Intercept	-2.03	0.18072
	Slope	1.52178	0.18018

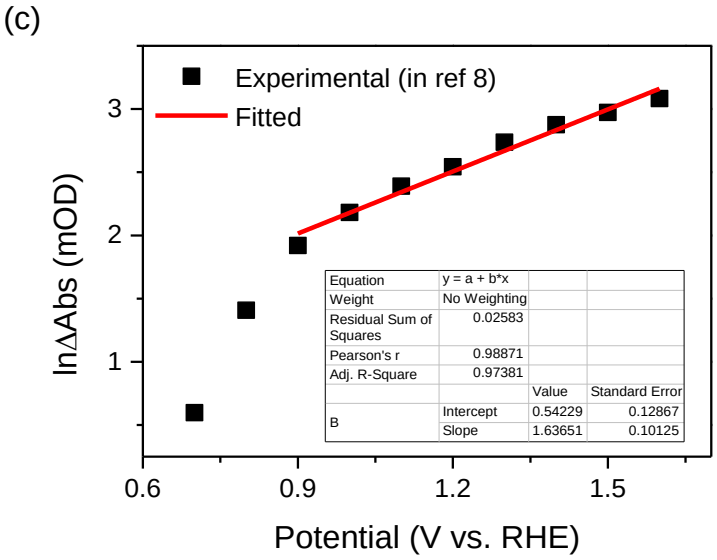

Supplementary Figure 6. Absorption difference measured at 580 nm as a function of applied bias for the hematite-based photoanode which is derived from spectroelectrochemistry results in the dark as reported previously. **(a)** α-Fe_2O_3 electrodes results from the **Figure 5**a and c in **ref**[6]; **(b)** CoO_x surface modified α-Fe_2O_3 electrodes results from the **Figure 5**b and c in **ref**[6]; **(c)** α-Fe_2O_3 electrodes results from the **Figure 5**a and c in **ref**[8].

10 Cyclic voltammetry (CV) measurements

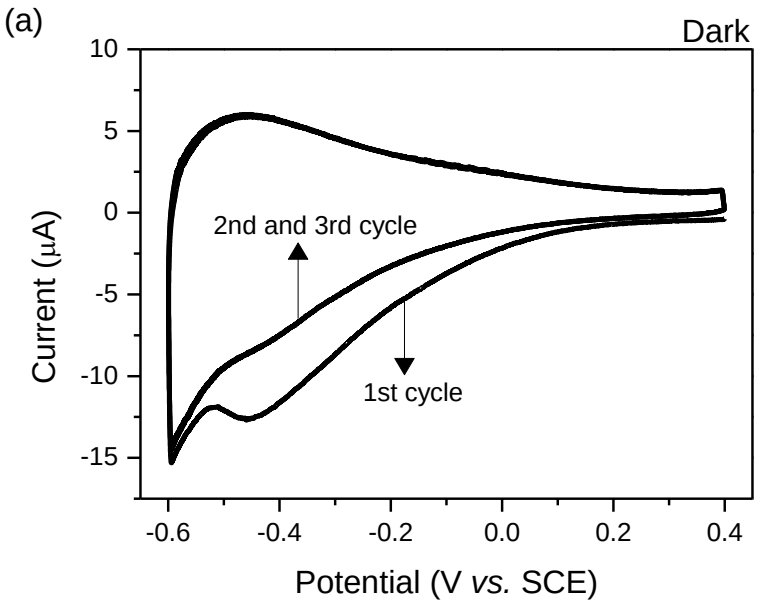

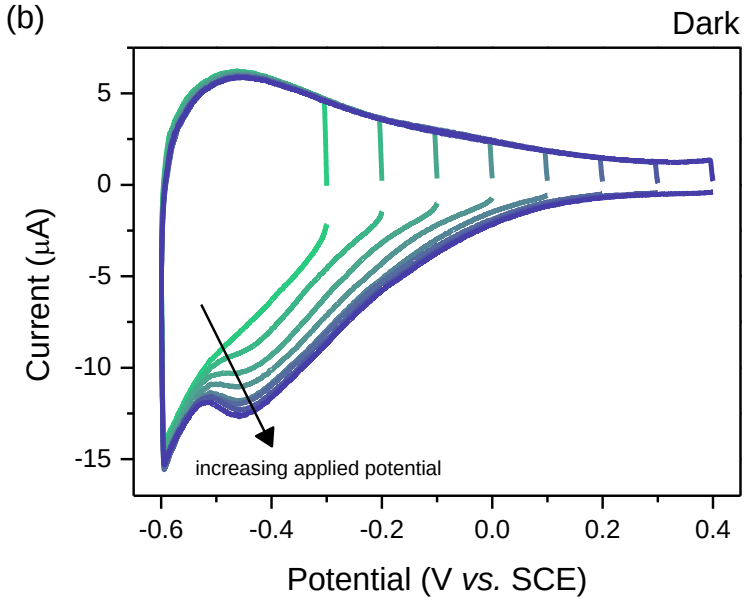

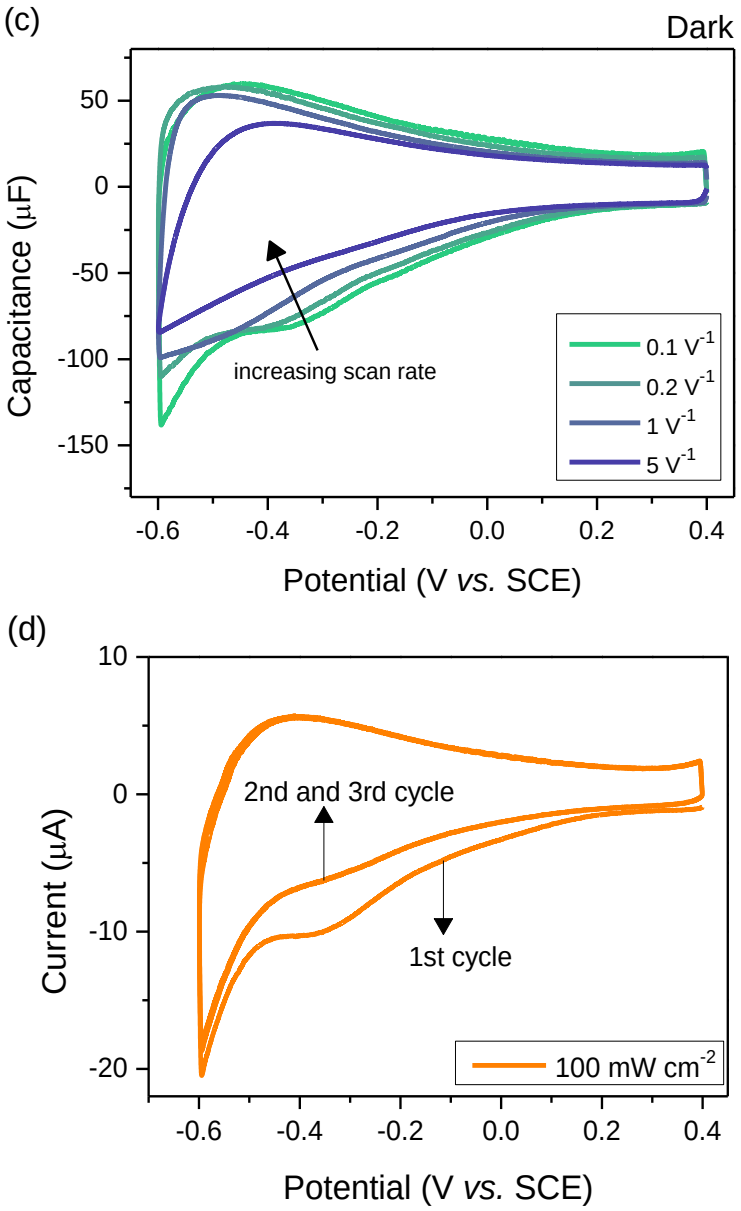

Supplementary Figure 7. Fast cathodic CV scans (0.1 V s^{-1}, otherwise separately labeled) of the α-Fe_2O_3 electrodes in the dark at pH 13.8 after preconditioning at high potential for 3 min. **(a)** comparison of different scan cycles; **(b)** comparison of the first cycle measured at different potential; **(c)** the capacitive plot of different scan rates (0.1, 0.2, 0.5 V s^{-1}); **(d)** CV scans under illumination of 100 mWcm^{-2} and other condition are the same as **(a)**.

11 Transient absorption spectroscopy (TAS) results

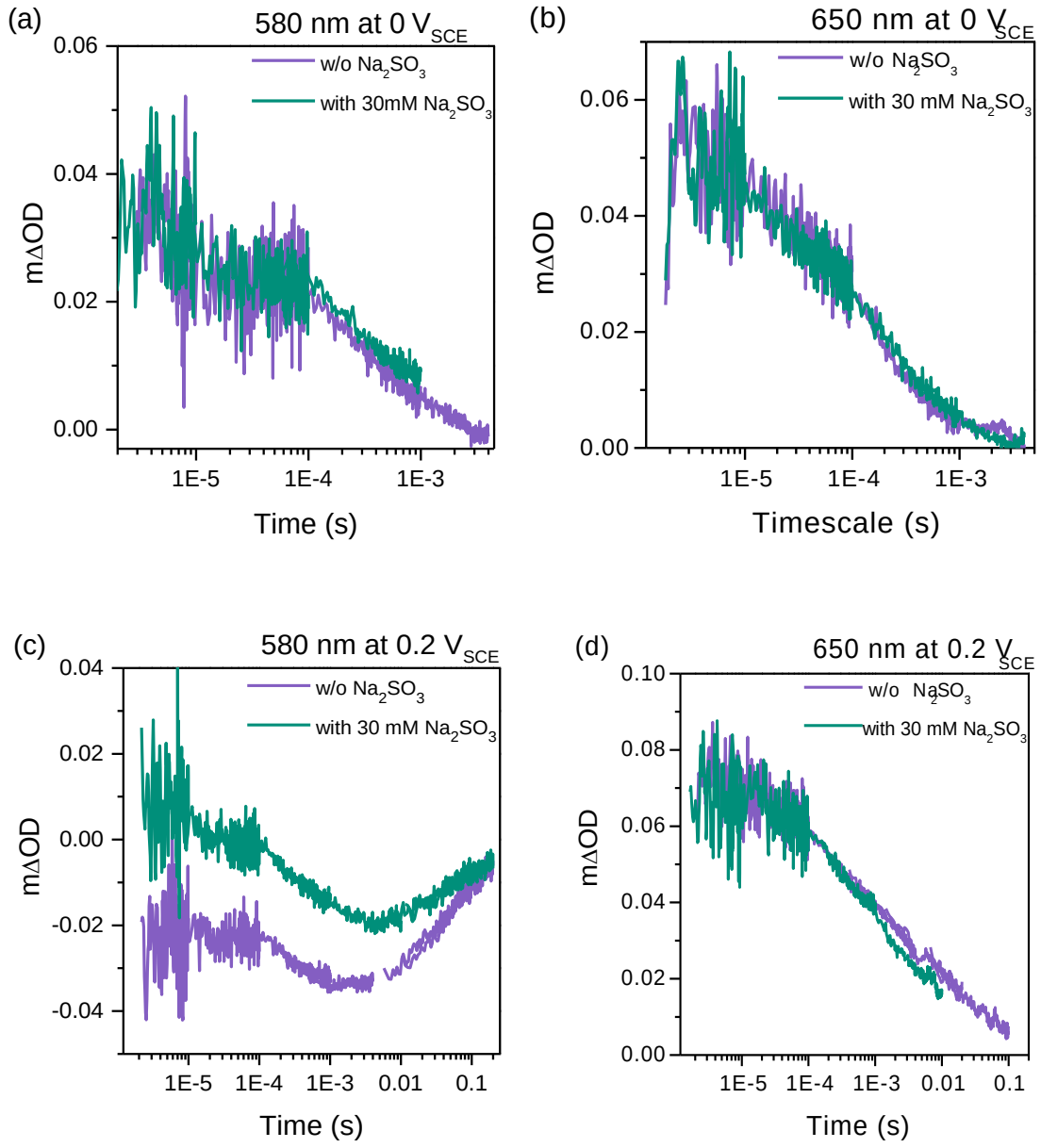

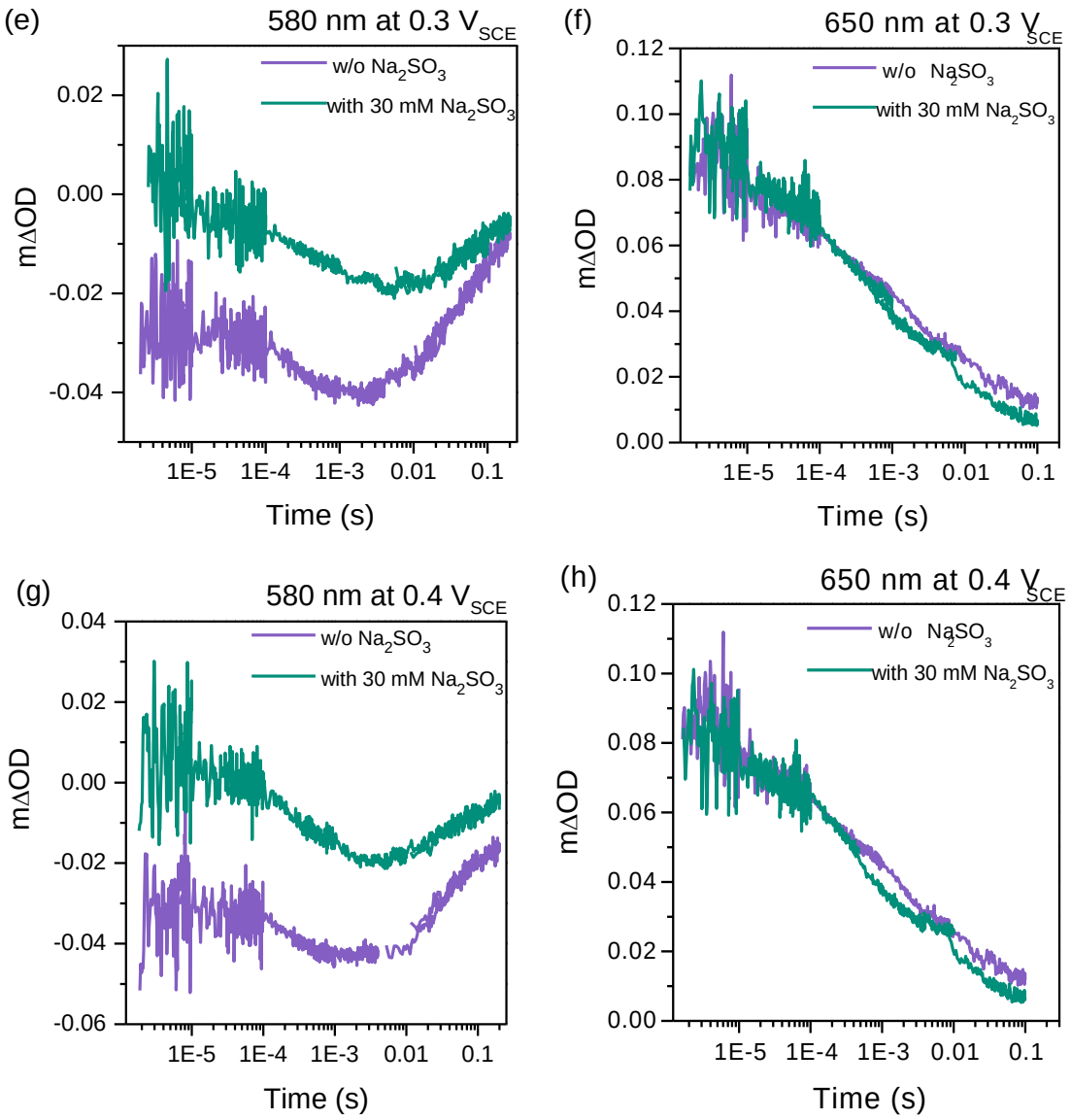

Supplementary Figure 8. TAS decay results. Comparison of TAS for the with and without 30 mM Na_2SO_3 probed at 580 nm **(a, c, e, g)** and 650 nm **(b, d, f, h)** at different potential: (a), (b) at 0 V_{SCE}; (c), (d) at 0.2 V_{SCE}; (e), (f) at 0.3 V_{SCE}; (g), (h) at 0.4 V_{SCE}.

12 Electrochemical impedance spectroscopy (EIS) results

Typical EIS response of the α-Fe_2O_3 electrodes obtained as a function of applied potential at different light intensity in 1 M NaOH at 100 mW cm^{-2} is presented in

Supplementary Figure 9a-d**.** According to previous reports[21, 22, 27, 29], the second semicircle on Nynquist plots can be assigned to photoelectrochemical reaction process. Therefore, k_{ct} equals to the angular frequency of the maximum imaginary component($\omega^1_{\max}$) of the second semicircle arc on Nynquist plots, which can be obtained by mathematic fitting of equation 23 in **Ref**[20]. Note that the $\omega^1_{\max}$ can be directly determined from the Nyquist plots during the maximum frequency range as illustrated in **Supplementary Figure 9**c (red dotted circle). As presented in **Supplementary Table 2**, the $\omega^1_{\max}$ derived by mathematic fitting in good match with that directly obtained from the Nyquist plots. This consistency supports the appropriateness of the derived k_{ct}. Thus, we can use k_{ct} to verify the proposed kinetic model. Satisfactory results have been achieved between the actual case and the theoretic expectation of model, even for the less potential independence ω^1_{max} observed at high anodic potential (**Figure 3**c and **Supplementary Figure 9**e). According to **Supplementary eq.(14)**, the less potential independence ω^1_{max} may be caused by two reasons: **1)** the C_{SC} is further decreased at high anodic potential, leading to even smaller $C_{\mathrm{SC}}/C_{\mathrm{H}}$; **2)** the faster k_{ct} at high anodic potential compared to that at lower applied potential would accelerate photohole transfer, which results in decreased accumulation of photoholes, bringing about smaller $\beta q p^0_{\mathrm{ss}}/\kappa_{\mathrm{B}} T C_{\mathrm{H}}$. All these factors may contribute to less increase in the amplitude of φ_{H} with respect to that at lower applied potential, consequently resulting in the potential independent k_{ct}. Besides, as shown in **Supplementary Figure 9**f, a good linear correlation between ω^1_{max} and j_{st} was

observed at strong light intensity of 100 mW cm^{-2}, consistent with the theoretic prediction of **Supplementary eq.(14)**. From the slope of ω_{max}^{1} *vs.* j_{st} curve, the C_H are determined to be 120 μF cm^{-2} for α-Fe_2O_3 electrodes in 1 M NaOH, which further validate the estimation of N_{trap} by the positively shifted E_{fb} in **Supplementary Figure 3**a.

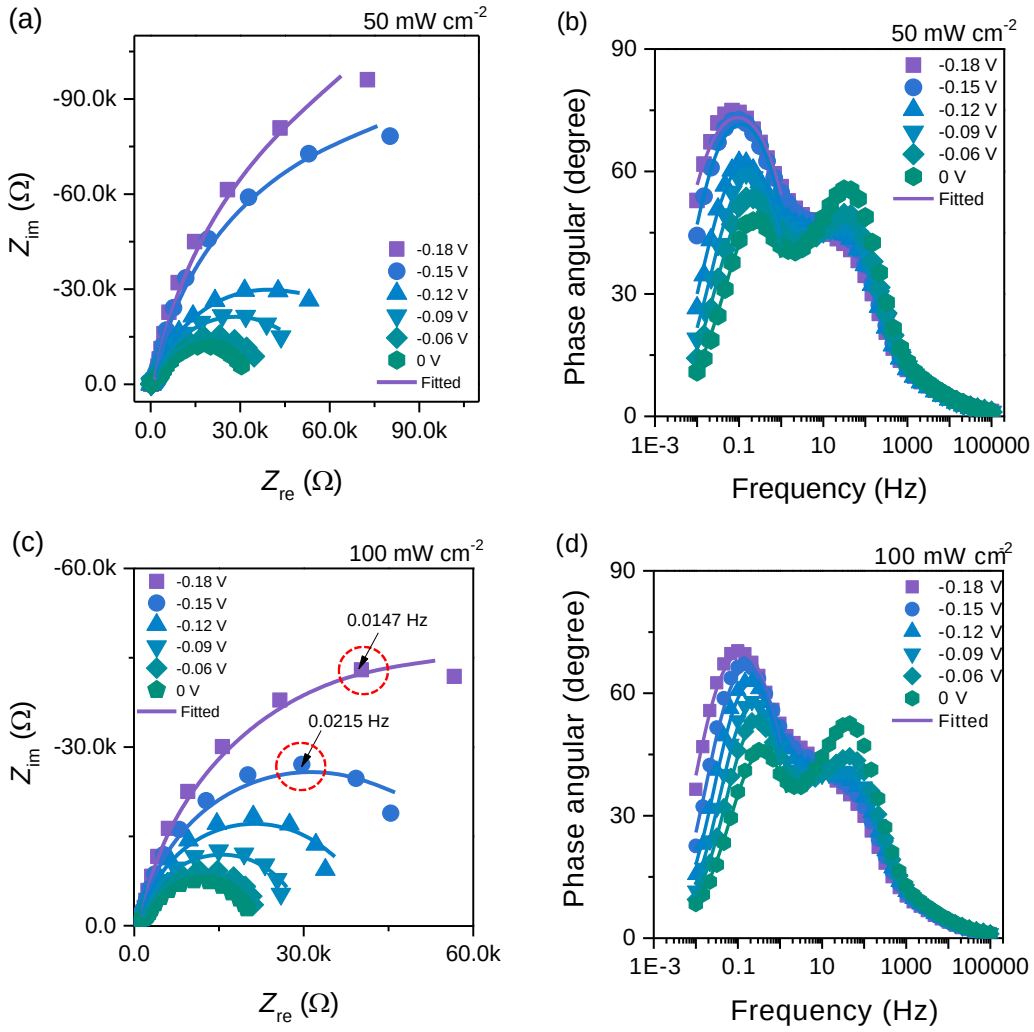

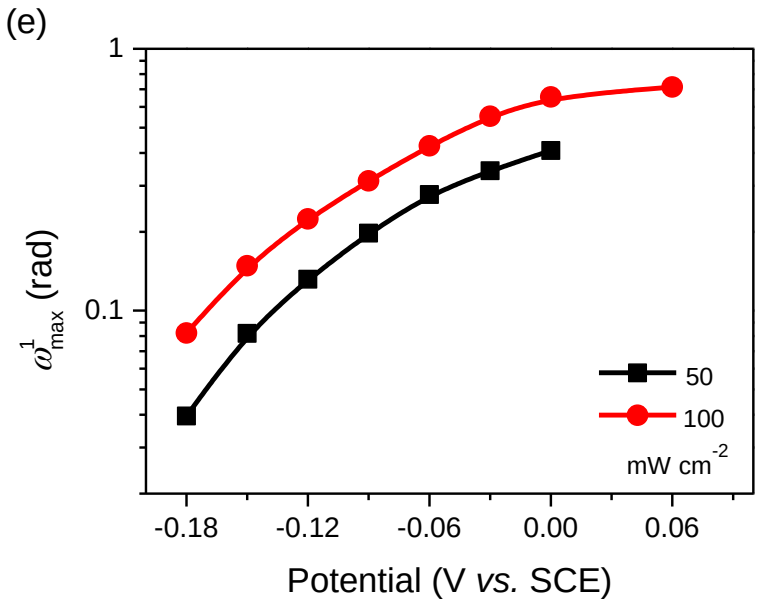

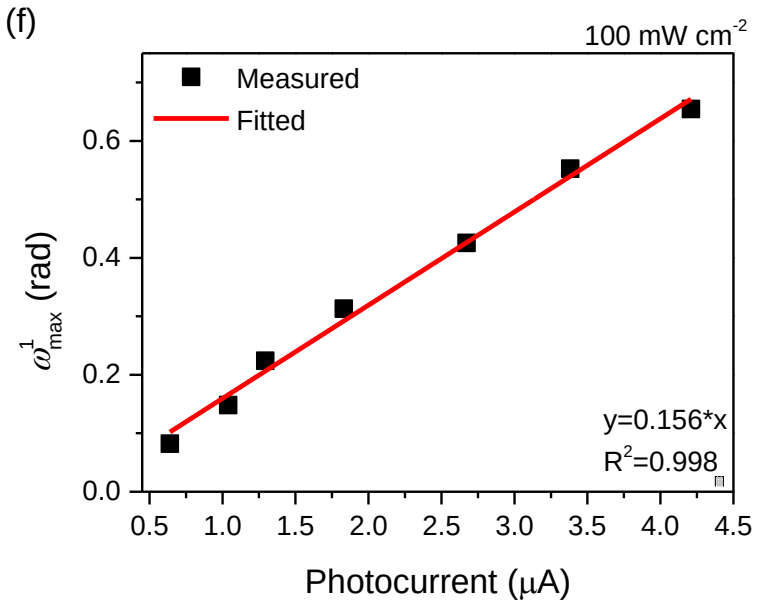

Supplementary Figure 9. EIS measurement results. Typical EIS responses of the α-Fe_2O_3 electrodes under illumination at different light intensities (50, 100 mW cm^{-2}): **(a)(c)** Nynquist plots and **(b)(d)** Bode plots. The data in line were used to derive ω^1_{max} by fitting equation 23 in **Ref[20]**; **(e)** influence of potential on the ω^1_{max} for the α-Fe_2O_3 electrode at at different light intensities (50, 100 mW cm^{-2}); **(f)** curves of the ω^1_{max} *vs.* j_{st} of the α-Fe_2O_3 electrodes at 100 mW cm^{-2}.

Supplementary Table 2. Comparison of the ω^1_{max} obtained by mathematic fitting and directly determined from EIS data at 100 mW cm^{-2} in the electrolyte of pH 13.8

Potential/ V vs. SCE	ω^1_{max} by mathematic fitting/ s^{-1}	ω^1_{max} directly determined from EIS data points ($2\pi f$) / s^{-1}
-0.18	0.08209	0.09236 (0.0147 Hz)
-0.15	0.14826	0.13509 (0.0215 Hz)
-0.12	0.22394	0.19792 (0.0315 Hz)
-0.09	0.31312	0.29154 (0.0464 Hz)
-0.06	0.42569	0.42789 (0.0681 Hz)
0	0.55252	0.62832 (0.1 Hz)

References

1. Iandolo B, Hellman A. The role of surface States in the oxygen evolution reaction on hematite. *Angew Chem Int Ed Engl* **53**, 13404-13408 (2014).

2. Yatom N, Neufeld O, Caspary Toroker M. Toward Settling the Debate on the Role of Fe2O3 Surface States for Water Splitting. *J Phys Chem C* **119**, 24789-24795 (2015).

3. Zhang J, Lin Q, Wang Z, Liu H, Li X, Zhang Y. Identifying Water Oxidation Mechanisms at Pure and Titanium-Doped Hematite-Based Photoanodes with Spectroelectrochemistry. *Small Methods* **5**, e2100976 (2021).

4. Cummings CY, Marken F, Peter LM, Wijayantha KG, Tahir AA. New insights into water splitting at mesoporous alpha-Fe2O3 films: a study by modulated transmittance and impedance spectroscopies. *J Am Chem Soc* **134**, 1228-1234 (2012).

5. Klahr B, Hamann T. Water Oxidation on Hematite Photoelectrodes: Insight into the Nature of Surface States through In Situ Spectroelectrochemistry. *J Phys Chem C* **118**, 10393-10399 (2014).

6. Barroso M, *et al.* Dynamics of photogenerated holes in surface modified alpha-Fe2O3 photoanodes for solar water splitting. *Proc Natl Acad Sci USA* **109**, 15640-15645 (2012).

7. Barroso M, Cowan AJ, Pendlebury SR, Gratzel M, Klug DR, Durrant JR. The role of cobalt phosphate in enhancing the photocatalytic activity of alpha-Fe2O3 toward water oxidation. *J Am Chem Soc* **133**, 14868-14871 (2011).

8. Barroso M, Pendlebury SR, Cowan AJ, Durrant JR. Charge carrier trapping, recombination and transfer in hematite (α-Fe2O3) water splitting photoanodes. *Chem Sci* **4**, 2724-2734 (2013).

9. Le Formal F, Pendlebury SR, Cornuz M, Tilley SD, Gratzel M, Durrant JR. Back electron-hole recombination in hematite photoanodes for water splitting. *J Am Chem Soc* **136**, 2564-2574 (2014).

10. Mesa CA, *et al.* Impact of the Synthesis Route on the Water Oxidation Kinetics of Hematite Photoanodes. *J Phys Chem Lett* **11**, 7285-7290 (2020).

11. Braun A, *et al.* Direct Observation of Two Electron Holes in a Hematite Photoanode during Photoelectrochemical Water Splitting. *J Phys Chem C* **116**, 16870-16875 (2012).

12. Zandi O, Hamann TW. Determination of photoelectrochemical water oxidation intermediates on haematite electrode surfaces using operando infrared spectroscopy. *Nat Chem* **8**, 778-783 (2016).

13. Klahr B, Gimenez S, Fabregat-Santiago F, Bisquert J, Hamann TW. Electrochemical and photoelectrochemical investigation of water oxidation with hematite electrodes. *Energy Environ Sci* **5**, (2012).

14. Klahr B, Gimenez S, Fabregat-Santiago F, Hamann T, Bisquert J. Water oxidation at hematite photoelectrodes: the role of surface states. *J Am Chem Soc* **134**, 4294-4302 (2012).

15. Li J, *et al.* Reaction kinetics and interplay of two different surface states on hematite photoanodes for water oxidation. *Nat Commun* **12**, 255

(2021).

16. Shangguang pengpeng, Tong Shaoping, Li Haili, Wenhua. L. Influence of the Potential on the Charge-Transfer Rate Constant of Photooxidation of Water over alpha-Fe_2O_3 and Ti-Doped alpha-Fe_2O_3.

17. Klotz D, Grave DA, Rothschild A. Accurate determination of the charge transfer efficiency of photoanodes for solar water splitting. *Phys Chem Chem Phys* **19**, 20383-20392 (2017).

18. G. Oskam JCS, P. M. Hoffmann, P. C. Searson*. Electrical Properties of n-Type (111) Si in Aqueous K4Fe(CN)6 Solution. *J Electrochem Soc* **143**, 2531-2537 (1996).

19. Peter M. Hoffmann GO, and Peter C. Searson. Analysis of the impedance response due to surface states at the semiconductor/solution interface. *J Appl Phys* **83**, 4309-4323 (1998).

20. Leng WH, Zhang Z, Zhang JQ, Cao CN. Investigation of the Kinetics of a TiO2 Photoelectrocatalytic Reaction Involving Charge Transfer and Recombination through Surface States by Electrochemical Impedance Spectroscopy. *J Phys Chem B* **109**, 15008-15023 (2005).

21. Zhang S, Shangguan P, Tong S, Zhang Z, Leng W. Enhanced Photoelectrochemical Oxidation of Water over Ti-Doped α-Fe2O3 Electrodes by Surface Electrodeposition InOOH. *J Phys Chem C* **123**, 24352-24361 (2019).

22. Zhang S, Zhang Z, Leng W. Understanding the enhanced photoelectrochemical water oxidation over Ti-doped α-Fe2O3 electrodes by electrochemical reduction pretreatment. *Phys Chem Chem Phys* **22**, 7835-7843 (2020).

23. Upul Wijayantha KG, Saremi-Yarahmadi S, Peter LM. Kinetics of oxygen evolution at alpha-Fe2O3 photoanodes: a study by photoelectrochemical impedance spectroscopy. *Phys Chem Chem Phys* **13**, 5264-5270 (2011).

24. Nishida M. Charge transfer by surface states in the photoelectrolysis of water using a semiconductor electrode. *Nature* **277**, 202-203 (1979).

25. Peter LM, Walker AB, Bein T, Hufnagel AG, Kondofersky I.

Interpretation of photocurrent transients at semiconductor electrodes: Effects of band-edge unpinning. *J Electroanal Chem* **872**, (2020).

26. Wang G, *et al*. Facile Synthesis of Highly Photoactive a-Fe2O3-Based Films for Water Oxidation. *Nano Lett* **10.1021**, 3503–3509 (2011).

27. Shangguan P, Tong S, Li H, Leng W. Enhanced photoelectrochemical oxidation of water over undoped and Ti-doped alpha-Fe_2O_3 electrodes by electrochemical reduction pretreatment. *RSC Adv* **10163**, 10163–10167 (2013).

28. Zhang S, Gao B, Leng W. Kinetic Difference in Water Photooxidation between TiO2 and WO3 Electrodes by Rate Law Analysis. *ACS Appl Energy Mater* **6**, 1973-1981 (2023).

29. Shangguan P-P, Tong S-P, Li H-L, Leng W-H. Influence of the Potential on the Charge-Transfer Rate Constant of Photooxidation of Water over α-Fe2O3 and Ti-Doped α-Fe2O3. *Acta Phys Chim Sin* **29**, 1954-1960 (2013).

30. Glasscock JA, Barnes PRF, Plumb IC, Savvides N. Enhancement of Photoelectrochemical Hydrogen Production from Hematite Thin Films by the Introduction of Ti and Si. *J Phys Chem C* **111**, 16477-16488 (2007).